Substrate-dependent synergistic many-body effects in atomically thin two-dimensional WS$_2$

Shreyasi Das,[1] Rup K. Chowdhury,[2,*] Debjani Karmakar [ORCID],[3] Soumen Das,[4] and Samit K. Ray [ORCID][2,†]

[1]*School of Nano Science and Technology, Indian Institute of Technology Kharagpur, Kharagpur 721302, India*
[2]*Department of Physics, Indian Institute of Technology Kharagpur, Kharagpur 721302, India*
[3]*Technical Physics & Prototype Engineering Division, Bhabha Atomic Research Center, Mumbai 400085, India*
[4]*School of Medical Science and Technology, Indian Institute of Technology Kharagpur, Kharagpur 721302, India*

Mott transition has been realized in atomically thin monolayers (MLs) of two-dimensional (2D) semiconductors (WS$_2$) via optically excited carriers above a critical carrier density through many-body interactions. The above nonlinear optical transition occurs when excited electron hole pairs in the ML WS$_2$ continuum heavily interact with each other followed by transformation into a collective electron-hole-plasma phase, by losing their identity as individual quasiparticles. This is manifested by the alluring redshift-blueshift crossover phenomena of the excitonic peaks in the emission spectra, resulting from the synergistic attraction-repulsion processes at the Mott transition point. A systematic investigation of many-body effects is reported on ML WS$_2$, while considering the modulated dielectric screening of three different substrates, viz., silicon dioxide, sapphire, and gold. Substrate doping effects on ML WS$_2$ are discussed using the Raman fingerprints and photoluminescence spectral weight, which are further corroborated using theoretical density functional theory calculations. Further, the substrate-dependent excitonic Bohr radius of ML WS$_2$ is extracted via modeling the emission energy shift with Lennard-Jones potential. The variation of the Mott point, as well as the excitonic Bohr radius, is explained via the substrate-induced dielectric screening effect for both dielectric substrates, which is, however, absent in ML WS$_2$ on Au. In this paper, we therefore reveal diverse many-body ramifications in 2D semiconductors and offer decisive outlooks on selecting impeccable substrate materials for innovative device engineering.

I. INTRODUCTION

Excitonic complex-induced many-body phenomena control the optical and electrical properties of two-dimensional (2D) semiconducting transition metal dichalcogenides (TMDs), making them inimitable candidates for nanoelectronics [1,2], nanophotonics [3,4], optoelectronics [5–7], and valleytronics [8–10] devices. The optical properties of TMDs are strongly influenced by the dielectric environment and thus are dependent on the choice of substrates, which vary widely depending upon the end applications [11–13]. The Coulomb potential inside photogenerated excitonic quasiparticles and many-body phenomena are strongly affected via environmental dielectric permittivity, as the electric line of forces extend beyond the boundaries of atomically thin 2D TMD layers [14,15]. These substrate-induced Coulomb-screening effects lead to bandgap renormalization and binding energy reduction of excitons in 2D monolayers, whereas substrate-induced unintentional carrier doping plays a significant role in the emission spectral weight, providing a wide design flexibility of 2D-material-based

optical devices [16–19]. A comparative study with suspended MoS$_2$ flakes has addressed the substrate-induced doping effects on photoluminescence (PL) emission [18], while the effect of dielectric screening on the emission characteristics of the WS$_2$ monolayer on different substrates [20] could be explained with band renormalization phenomena. However, a detailed investigation on the substrate-induced many-body effects at the high carrier density regime is still lacking on 2D TMDs.

The modulation of strain [1], carrier density [21,22], dielectric environment [23,24], and variation of temperature [25,26] play important roles in altering the many-body effects in a 2D system, giving rise to the appearance of higher-order bound states (e.g., trions), line shift of quasiparticle resonance, and anomalous behavior in the emission spectral weight of quasiparticles [26]. With increasing electron-hole densities from photogenerated carrier doping, the Coulombic potential between charges gets efficiently screened due to the exchange and correlation effect, leading to bandgap renormalization and the reduction of the binding energy of quasiparticles [27–29]. On the other hand, in the high carrier density regime, excitons start to interact with each other and lose their identity to create a new collective phase called electron-hole-plasma (EHP) [30]. This transition from an insulating gas of excitons at lower densities to a metal like EHP state at higher carrier densities is attributed to the Mott transition. At a critical density (n_M), where the Mott transition takes place, the number of excitons become so high that the average distance between

them decreases to their exciton Bohr radius (r_B) [31] limit. Further, in this critical density regime, the conductivity of the material undergoes a percolation-driven metal-insulator transition, which can be realized via temperature-dependent transport behavior in 2D layered systems [32–34]. The coexistence of different many-body effects at an elevated carrier concentration can lead to an anomalous redshift-blueshift crossover (RBC) of excitonic resonance, which was reported earlier in the case of optical doping via transient absorption spectroscopy [35,36], though their steady-state emission characteristics are yet to be addressed. Due to the reduced dimensionality and relatively longer lifetime (in picoseconds) of excitonic complexes, a higher carrier density is achievable in 2D TMDs even with a continuous wave laser beam excitation in steady state [37,38]. Moreover, the effect of various dielectric environments on 2D TMDs at the Mott transition point opens possibilities for device fabrication [39].

In this paper, we report a comparative study on many-body quasiparticle phenomena for 2D monolayer (ML) WS$_2$ flakes on two different dielectric substrates (SiO$_2$ and Al$_2$O$_3$) and a metallic (Au) substrate through emission and Raman spectroscopy techniques. We established a correlation between (i) carrier density induced and (ii) substrate-dependent many-body effects on ML WS$_2$. The anomalous behavior in PL spectral weight variation and resonance peak shift associated with the increase of optical doping (*n*-type) and dielectric screening are discussed for all three samples. The RBC of the excitonic peaks is clearly observed for the high carrier density regime ($\sim 2 \times 10^{12}$ to 3×10^{12} cm^{-2}) at the Mott transition point for the insulating (SiO$_2$/Si and Al$_2$O$_3$) substrates, which is absent for the Au substrate. The origin of these RBC phenomena is further elucidated using band renormalization due to interplay between two distinct many-body effects: (i) Coulomb screening and (ii) Pauli blocking. Analogous to the hydrogen atom model, RBC is explained beyond the Mott density regime from the attraction-repulsion crossover of exciton-exciton interactions in 2D WS$_2$, which provides an estimation of the excitonic Bohr radius of WS$_2$ with varying dielectric environments.

II. EXPERIMENTAL METHODS: SYNTHESIS AND CHARACTERIZATION

Monolayer WS$_2$ flakes were obtained by mechanical exfoliation from a commercial WS$_2$ crystal (2D Semiconductors, Inc. Scottsdale, AZ, USA) using Scotch Magic Tape (3M Inc. USA) and directly exfoliated onto three substrates from the tape, as schematically described in Fig. S1 of the Supplemental Material [40]. Pieces of commercially purchased 300-nm-thick SiO$_2$ on highly doped Si wafers (1×1 cm^2) were cleaned with acetone, propanol, and deionized (DI) water in an ultrasonic bath followed by N$_2$ gun drying. The commercially available mirror polished Al$_2$O$_3$ substrates were also cleaned by acetone and DI water in an ultrasonic bath to remove dust and contaminants. On the other hand, the Au-coated SiO$_2$/Si substrate was fabricated by the physical vapor deposition technique with e-beam evaporation of Au using a HIND HIVAC system. A 10-nm-thick Au layer was grown on a clean SiO$_2$ substrate before exfoliation. Direct exfoliation of WS$_2$ on different substrates was employed in-

tentionally to avoid any extra doping inside the material from polymer-assisted dry or wet transfer techniques. An optical microscope [DM 2500M with a 100×, 0.9 numerical aperture (NA) objective, Leica] equipped with a color camera was used to locate and identify the monolayer WS$_2$ sheets with the naked eye. Optical contrast-based identification of ML WS$_2$ was performed using optical imaging in reflection geometry combined with image analysis software (IMAGEJ) [41,42]. The optical contrast profiles were generated using IMAGEJ in the R-channel grayscale image, which confirms the formation of ML WS$_2$ flakes on different substrates. Further, atomic force microscopy (AFM; Agilent Technology, Model: 5500) was used to image the WS$_2$ sheets in tapping mode in air to confirm the layer number by measuring the thickness of the nanosheets. The corresponding AFM topological images and line scan height profiles of the WS$_2$ flakes reconfirmed the monolayer exfoliation, with the thickness of the flake being ~ 0.8 nm [43]. Detailed investigations of substrate-induced effects on material characteristics were carried out by Raman and PL spectroscopy techniques, using a fiber coupled confocal micro-Raman/PL spectrometer (WITec alpha-300R, Inc. Ulm, Germany) with a continuous wave 532 nm laser excitation source. Room-temperature power-dependent PL study was performed using a 100× objective (0.8 NA) with diffraction limited laser spot size of ~ 0.5 μm. The power of the laser was calibrated using an optical power meter from Newport (model no: 1916-R; MKS Instruments, Inc.).

III. RESULTS AND DISCUSSIONS

ML WS$_2$ flakes were mechanically exfoliated from a commercially available bulk crystal using Scotch Magic Tape (3M) and directly transferred onto freshly cleaned substrates: (a) crystalline sapphire (Al$_2$O$_3$), (b) dielectric SiO$_2$/Si (oxide thickness ~ 285 nm), and (c) conducting Au-coated (~ 10 nm) SiO$_2$/Si substrate, as schematically shown in Figs. 1(a)–1(c). Here, the direct exfoliation of ML WS$_2$ on each substrate is confirmed by (i) The optical micrographs, (ii) R-channel grayscale images with contrast profiles, and (iii) AFM topography images along with height profiles of Figs. 1(a)–1(c). Further, the Raman mappings of the in-plane $E^1_{2g}(M)$ mode (~ 351 cm^{-1}) of WS$_2$ flakes on all three substrates are illustrated in Figs. 1(a)(iv)–1(c)(iv), where the green dashed areas are the ML region with reduced Raman intensity compared with their bulk counterparts [44]. A comparative Raman study for all samples is presented in Fig. 2(a) with the intense in-plane $E^1_{2g}(M)$ Raman peaks at ~ 351 cm^{-1} and the out-of-plane vibrational peaks A_{1g} at ~ 421 cm^{-1} [45]. With the variation of substrate, a clear shift of the out-of-plane (A_{1g}) vibrational Raman modes is recorded, as shown in Fig. 2(c). The softening of the A_{1g} peak in the Raman spectrum with substrate variation has a direct correlation with the charge transfer mechanism in 2D TMDs [46]. The increased electron doping leads to the filling-up of antibonding states of the conduction band (CB), mostly made up of d_z^2 orbitals of transition metal atoms, making the bonds weaker. Thus, the A_{1g} mode, which preserves the symmetry of the lattice, softens and reveals an increasing *n*-type doping in WS$_2$. The A_{1g} peak softens by 5.069 cm^{-1} from Au to the SiO$_2$/Si substrate, showing the
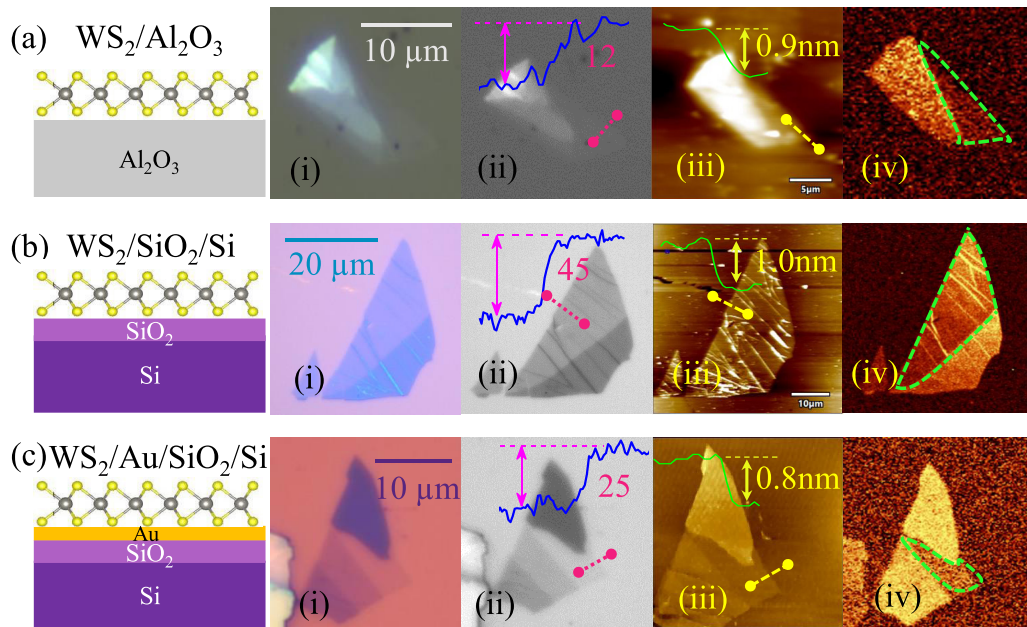
FIG. 1. (i) Optical microscopic image, (ii) R-channel grayscale image, (iii) atomic force microscopy (AFM) topographic image, and (iv) Raman mapping image (E_{2g}^1 peak) of corresponding monolayer (ML) WS$_2$ flakes on three substrates: (a) Al$_2$O$_3$ substrate, (b) SiO$_2$/Si substrate, and (c) Au/SiO$_2$/Si substrate. In the inset of the grayscale image (ii), a contrast profile has been shown along the pink dashed line, extracting data using IMAGE-J software and the height profile of the ML region shown in the inset of AFM topographic image (iii) along the yellow dashed line. The green dashed areas in Raman mapping images (iv) represent the ML region on each substrate.

increase in n-type doping in ML WS$_2$, as corroborated by the band structure calculation [Fig. 3] (detailed discussion in Appendix A).

Moreover, the PL spectral weight of ML WS$_2$ on various substrates may also differ because of the substrate-induced charge doping into the material. Comparing the normalized PL spectra of ML WS$_2$ for all samples [Fig. 2(b)], a broader emission peak with a full width at half maximum (FWHM) of 83.5 meV is perceived in the case of WS$_2$ on SiO$_2$/Si. To evaluate the substrate-induced variation of PL emission energy and spectral weight, we deconvoluted all the spectra into two Gaussian peaks to acquire optimal line shape of the excitonic quasiparticles for a fixed laser power density (P_d) $\sim$0.3 MW/cm^2, as depicted in Figs. 2(d)–2(f). The PL spectrum for WS$_2$/SiO$_2$/Si (k-SiO$_2 \sim 3.9$) [47] shows A-excitonic emission at $\sim$1.995 eV, corresponding to direct band-to-band transitions of ML WS$_2$ at the K (and/or K') point of the Brillouin zone, and trionic-A$^-$ emission at $\sim$1.965 eV with a binding energy of $\sim$30 meV, which are in good agreement with previously reported results of ML WS$_2$ [16,48]. However, for a higher-k dielectric substrate like Al$_2$O$_3$ ($k \sim 9$) [47], the A and A$^-$ peaks are found at 2.012 and 1.976 eV, respectively, which indicates that the PL peak energy of all quasiparticles gets blueshifted with increasing k value of the substrates. This blueshift of the resonance energy is a consequence of the dielectric screening-induced band renormalization and binding energy reduction (detailed discussion in Appendix B). The PL mapping images of A peaks [see top left inset of Figs. 2(d)–2(f)] reveal strong emissions from the ML regions of WS$_2$ on three different substrates. Further, the differential reflectivity plot of WS$_2$ on three substrates confirms the A-excitonic emission, as depicted in Fig. S2

of the Supplemental Material [40]. However, trion peaks are not realized from the room-temperature reflectivity spectra, in agreement with previous reports [14,42]. Moreover, in our room-temperature (300 K) PL and reflectivity measurements, the absence of the B-excitonic peak ($\sim$2.4 eV) has a direct consequence on large valence band splitting due to spin-orbit coupling (SOC) in ML WS$_2$. At 300 K, most of the carriers occupy the highest valence band maximum level containing higher density of states (DOS), resulting in the absence of B-excitonic PL even at a higher laser power [49]. The sublinear variation in the double logarithmic plot of the deconvoluted PL peak integrated intensity with laser power (Fig. S3 of the Supplemental Material [40]) confirms the neutral excitonic (A) and trionic (A$^-$) emission for all three substrates. It is important to emphasize that, for all three substrates, the integrated intensity variation of each peak is fitted with the power law equation only in the low power density regime to avoid photodoping-induced many-body effects. The extracted integrated intensity of quasiparticles from each deconvoluted spectrum is tabulated in Table I, from which we observe the trion-to-exciton integrated intensity ratio for SiO$_2$/Si, Al$_2$O$_3$, and Au/SiO$_2$/Si substrates to be 1.54, 0.62, and 0.42, respectively. Further, we have calculated the carrier concentration (n_e) in ML WS$_2$ from the integrated PL intensity ratio of trions to excitons using the law of mass action [43]:

$$ n_e = \left(\frac{I_{A^-}}{I_A}\right)\left(\frac{\gamma_A}{\gamma_{A^-}}\right)\left(\frac{4m_A m_e}{\pi \hbar^2 m_{A^-}}\right)(k_B T)\exp\left(\frac{E_b^{A^-}}{k_B T}\right), \quad (1) $$

where $\hbar$ is the reduced Planck's constant, k_B is the Boltzmann constant, $E_b^{A^-}$ is the trion binding energy, $m_A(m_{A^-})$ are the effective masses of exciton (trion), and $\gamma_A(\gamma_{A^-})$ are the radiative decay rates of excitons (trions). Here, $m_{A^-} = 2m_e + m_h$ and $m_A = m_e + m_h$, where m_e and m_h are the ef-
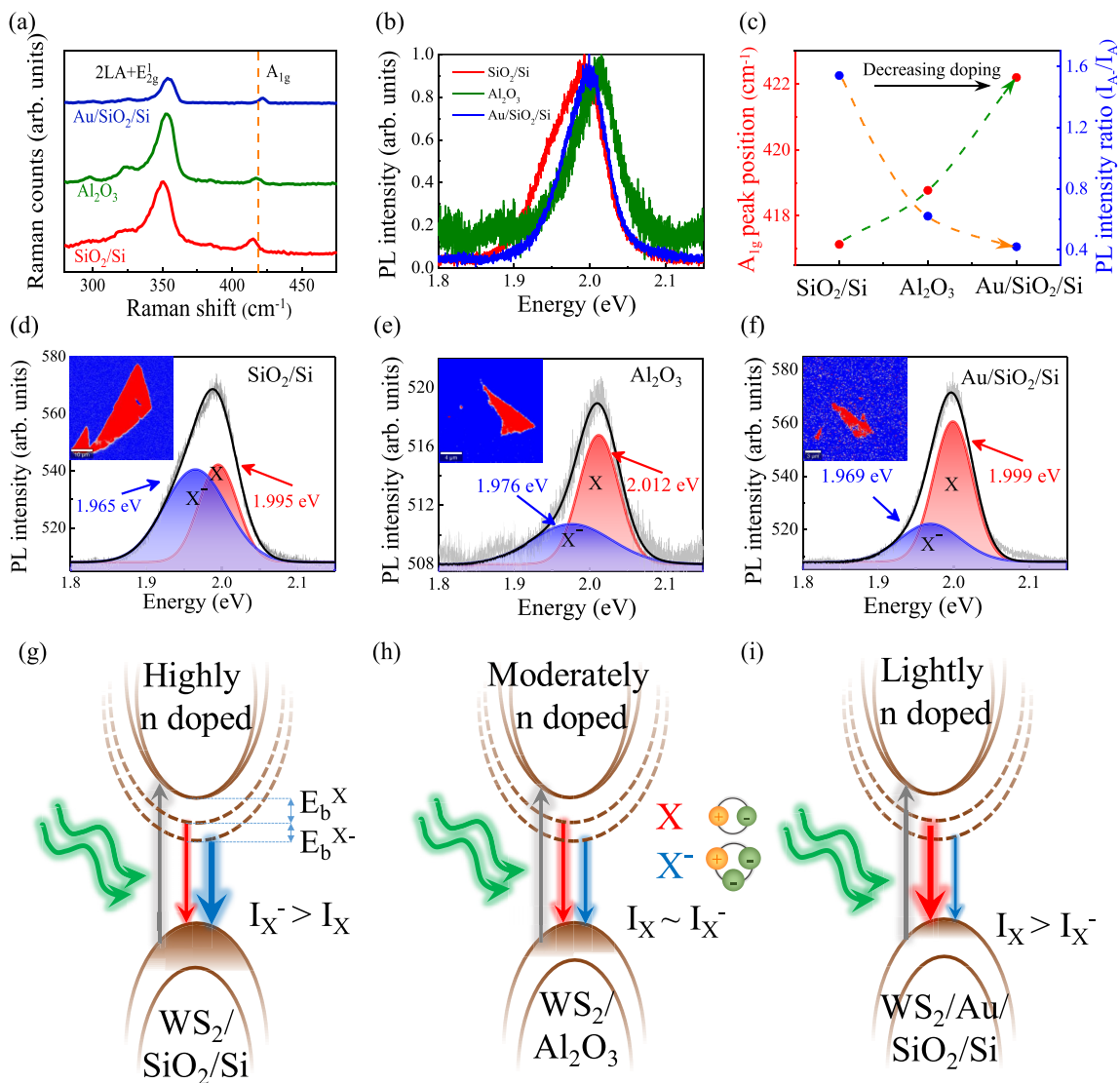
FIG. 2. (a) Comparative Raman spectra of monolayer (ML) WS$_2$ on all three substrates, collected at a very low laser power excitation (0.3 MW/cm^2). (b) Comparative normalized photoluminescence (PL) emission spectra at a low laser power density (0.3 MW/cm^2) of ML WS$_2$ flakes on three substrates: SiO$_2$/Si (red line), Al$_2$O$_3$ (green line), and Au/SiO$_2$/Si (blue line) showing clear peak shift and variation of full width at half maximum (FWHM). (c) The variation of A_{1g} Raman peak and PL intensity ratio of trion to exciton for different substrates, revealing substrate-induced doping. The green and orange dashed lines are drawn for the guidance of the eye. (d)–(f) Deconvoluted PL spectra of WS$_2$ on three different substrates, showing two distinct peaks corresponding to excitonic (red line) and trionic (blue line) emissions at a low laser power density ($\sim$0.3 MW/cm^2). The black line symbolizes the cumulative fit of two distinct peaks. The PL mapping of excitonic peak originating from the monolayer region is illustrated in the top left inset. (g)–(i) Schematic representation of substrate doping-induced exciton-to-trion intensity variation for SiO$_2$/Si, Al$_2$O$_3$, and Au/SiO$_2$/Si substrates, respectively.

fective masses of electrons and holes in WS$_2$, respectively. The corresponding areal carrier concentration (n_e) for above three substrates are found to be $\sim$3.62 $\times$ 10^{13}, 1.54 $\times$ 10^{13}, and 0.98 $\times$ 10^{13} cm^{-2} in ML WS$_2$, which contribute to the fraction of trion formation and spectral weight variation with changing substrate materials. As represented schematically in Fig. 2(g), for the SiO$_2$/Si substrate, the maximum carrier concentration (denoted by brown shade in the valence band) leads to the formation of a higher number of trions (blue arrow) than excitons (red arrow), and WS$_2$ behaves as highly n doped. In the case of the Al$_2$O$_3$ substrate, WS$_2$ can be considered moderately n doped with the formation of almost equal quantities of trions and excitons [Fig. 2(h)]. On the other

hand, due to draining of charges to the Au film, WS$_2$ on the Au/SiO$_2$/Si substrate behaves as lightly n doped with the exciton density greater than that of the trion, as depicted in Fig. 2(i). The existence of charged trions along with excitonic features is a consequence of the negative charge transfer due to unintentional substrate-induced doping in ML WS$_2$ for all samples at a low laser power density [50]. In general, electrons move toward a material with a lower Fermi level from that having a higher Fermi level, and the excess electrons inside the system interact with neutral excitons to form charged excitons or trions. The formation of a trion reduces the exciton density in the system, leading to a decrease in PL emission efficiency with the broadening of peak width. Therefore, a
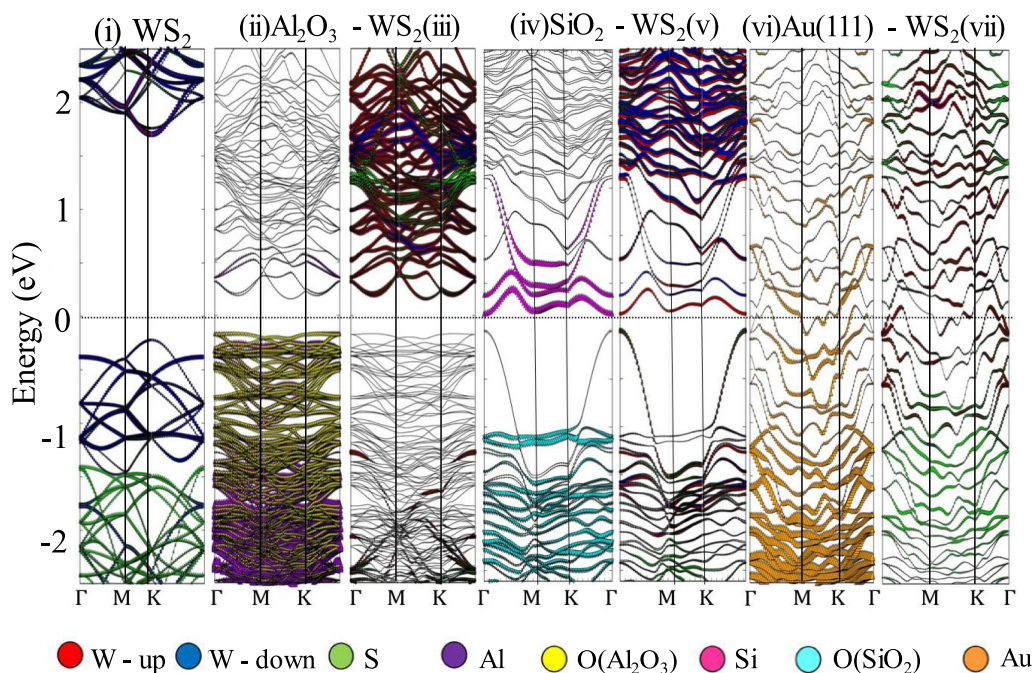
FIG. 3. Orbital-projected band structures (i) for WS_2 monolayer (ML) with W-up (up-spin channel), W-down (down-spin channel) $5d$ orbitals and S-$3p$ orbitals, (ii) Al-$3s$ and $3p$ and O-$2p$ projected bands for Al_2O_3/WS_2, (iii) W-up (up-spin channel), W-down (down-spin channel) $5d$ and S-$3p$ projected bands for Al_2O_3/WS_2, (iv) Si-$3s$ and $3p$ and O-$2p$ projected bands for SiO_2/WS_2, (v) W-up (up-spin channel), W-down (down-spin channel) $5d$ and S-$3p$ projected bands for SiO_2/WS_2, (vi) Au-$5d$ and $6s$ projected bands for Au[111]/WS_2, (vii) W-up (up-spin channel), W-down (down-spin channel) $5d$ and S-$3p$ projected bands for Au[111]/WS_2.

lower integrated intensity ratio between the trion (I_A^-) and exciton (I_A) signifies a lower n-doping level in monolayer WS_2, and the resultant PL efficiency is eventually dominated by neutral excitonic emission. As a result, the SiO_2 substrate induces the maximum n-type doping with the highest trion-to-exciton intensity ratio ($\sim$1.54) along with a greater FWHM than the other two substrates. Here, it may be noted that our theoretical density functional theory (DFT) calculations also suggested [Fig. 3] higher doping from the SiO_2 substrate than that of Al_2O_3, which is corroborated with the experimental findings. However, Au-coated SiO_2 substrate reveals the maximum n-type doping in our DFT studies. This can be explained via the metallic nature of the interface between Au and WS_2, as the photogenerated excess electrons inside ML WS_2 are transferred to the Au-coated substrate through the interface [Fig. 3]. Consequently, it hinders the trion formation processes in 2D WS_2, leading to the lowest trion-to-exciton intensity ratio of 0.42, as well as the reduced FWHM of the PL spectrum, as observed experimentally in our case.

For room-temperature realization of the Mott insulator-to-metal transition with investigation of many-body effects on the nature of excitonic quasiparticles and their substrate dependency, the intensity variation of PL emission and resonance peak shift have been investigated for each substrate with elevated carrier population by increasing the laser power density. This has a direct consequence on the many-body effects of ML WS_2. Here, it is important to mention that we purposefully carried out all the power-dependent PL measurements with an accumulation time of 0.5 s and 10 accumulations to avoid prolonged laser exposure-induced photodoping and sample damage during the experiment (detailed discussion in Supplemental Material Sec. S4 [40]). Moreover, we have also ensured collection of individual PL spectra at different locations on the ML WS_2 flakes for each laser power during the experiment. The power-dependent PL plots (Figs. 4(a)–4(c) and Figs. S5(a)–S5(c) of the Supplemental Material [40]) reveal that the emission intensity increases up to a maximum value and decreases thereafter with further increment of laser power for ML WS_2 on each substrate. This downfall in PL intensity is followed by a RBC for excitonic resonance peak in case of dielectric substrates (Al_2O_3 and SiO_2/Si). PL spectra with varying excitation power have been deconvoluted to understand the peak shift and spectral weight variation of individual quasiparticle with carrier density for all substrates

TABLE I. Substrate-induced charge doping.

Substrate	I_A	I_{A-}	$I_A : I_{A-}$	Doping	n_e (10^{13} cm^{-2})
SiO_2	3874.57	5989.36	1:1.54	Highly n-doped	3.62
Al_2O_3	774.80	478.80	1:0.62	Moderately n-doped	1.54
Au	6028.94	2538.43	1:0.42	Lightly n-doped	0.98
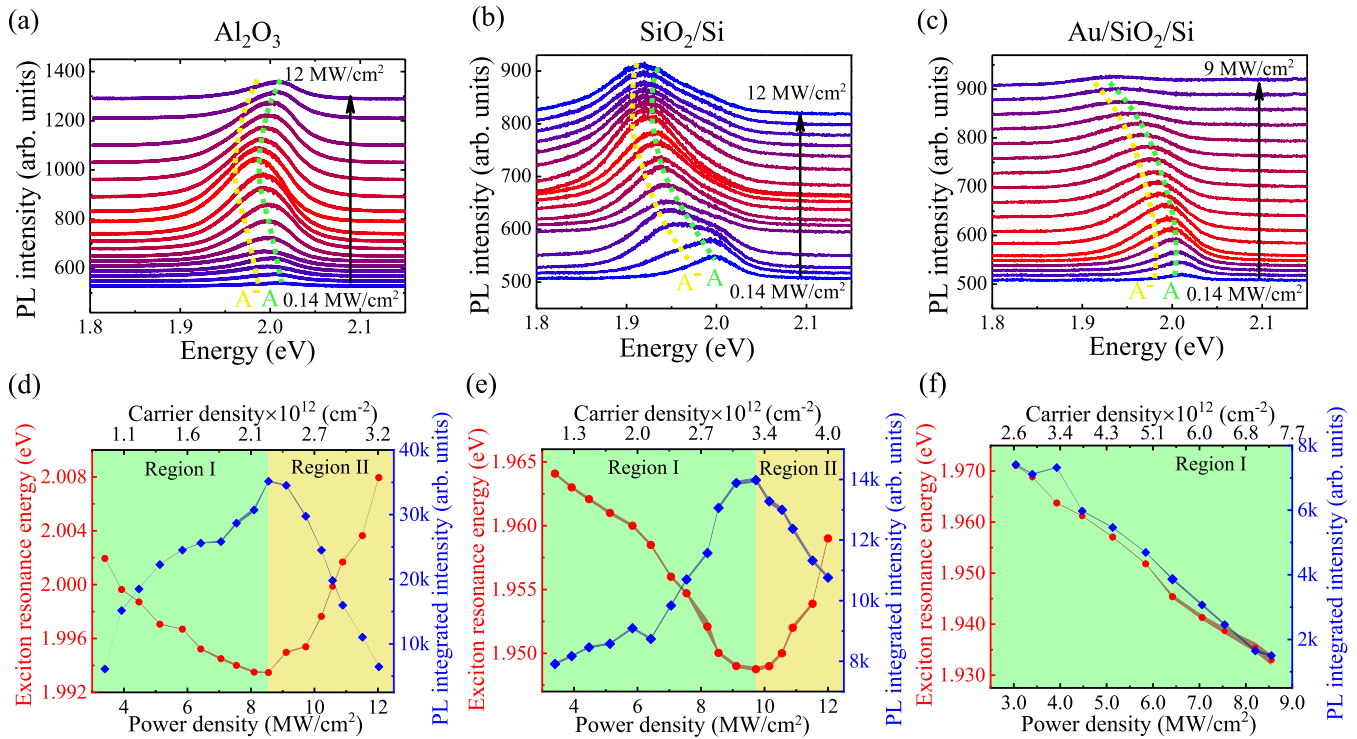
FIG. 4. Photoluminescence (PL) spectra of the monolayer (ML) WS$_2$ for different excitation powers on (a) Al$_2$O$_3$, (b) SiO$_2$/Si, and (c) Au/SiO$_2$/Si substrates. The color gradient signifies the intensity variation, i.e., first increases up to a maximum value (from blue to red) and then decreases further (from red to blue). The green (yellow) dotted line is a guide to the eye of exciton (trion) peak energy variation with laser power density. The variation of exciton resonance energy and integrated intensity (plotted for higher excitation power regime) with excitation-induced charge density in ML WS$_2$ on (d) Al$_2$O$_3$, (e) SiO$_2$/Si, and (f) Au/SiO$_2$/Si substrates. The redshift-blueshift crossover and integrated intensity fall of the exciton peak at the Mott transition point are indicated for dielectric substrates Al$_2$O$_3$ and SiO$_2$/Si via interface between two regions, Region I (green) and Region II (yellow).

(see Fig. S6 of the Supplemental Material [40]). At first, with increasing laser power, the redshift of PL peak is associated with two possible phenomena: band renormalization due to optical doping-induced charge screening effect and laser-induced temperature rise. However, the variation of emission characteristics via temperature increment of ML WS$_2$ due to laser exposure can be disregarded via qualitative discussions. The temperature increment would cause a redshift of the PL peak as well as an increase in its FWHM, although the peak shift is expected to be as low as $\sim$0.3 meV/K [51] compared with the carrier screening-induced peak shift of 4.82 meV MW^{-1} cm^{-2}, which we have observed at the lower power regime. Further increment of the laser power leads to a sudden fall in the integrated intensity (I_{PL}) of the exciton at $P_d \sim$8.55 MW/cm^2, followed by the RBC of the resonance peak in the case of ML WS$_2$ on Al$_2$O$_3$. For the SiO$_2$/Si substrate, the RBC phenomena and fall of intensity are perceived at $\sim$9.73 MW/cm^2 laser power density. This anomalous behavior in the case of two different dielectric substrates is advantageous for achieving a high carrier density via optical doping in ML WS$_2$, followed by the Mott insulator-to-metallic transition. It may be noted that the temperature-induced band renormalization effect fails to describe the origin of the blueshift of PL with increasing power density beyond the Mott point [52]. Hence, the laser-induced temperature increment effect is not the dominant one in comparison with other effects in the power-dependent optical study. On the other hand,

we have excluded the exciton-exciton annihilation (EEA) effect or nonradiative Auger recombination of the photogenerated carrier at very high exciton densities since the exciton density range studied for the investigation of the EEA phenomenon in TMDs is far less than the so-called Mott density ($\sim$10^{12} cm^{-2}), above which the contribution of EHP becomes dominant [53,54]. Furthermore, the EEA effect in 2D ML systems can be observed only in the first few picoseconds ($<$2 ps) of the exciton formation process under a relatively high pump fluence ($>$25 J/cm^2) [54], and hence, it cannot be realized in steady-state PL measurements. Therefore, the PL quenching phenomena and apparent bandgap shift toward a higher energy in the case of dielectric substrates can be explained via achieving the typical Mott carrier density in ML WS$_2$ at room temperature. Notably, for the ML WS$_2$ on the conducting surface (Au/SiO$_2$/Si), the fall in I_{PL} of excitonic emission happens at $P_d \sim$ 2 MW/cm^2 (Fig. S5 of the Supplemental Material [40]); however, the resonance peak position gets only redshifted without any RBC effect throughout our experimental laser power density range. This is attributed to the channeling of optically excited charge carriers of WS$_2$ through the metallic interface and consequently failing to achieve the Mott carrier density threshold.

Furthermore, the variation of the resonance peak position and integrated intensity of the A exciton around the critical Mott transition point is presented as a function of laser power density-induced carrier density (c_d) inside ML WS$_2$ for all

TABLE II. Substrate-dependent Mott transition point and Bohr radius.

Substrate	Mott point (MW/cm^2)	Carrier density (cm^{-2})	Redshift amount (meV/MW/cm^2)	Blueshift amount (meV/MW/cm^2)	Bohr radius (nm)
SiO$_2$/Si	9.73	3.267×10^{12}	4.82	4.51	2.686
Al$_2$O$_3$ (sapphire)	8.55	2.267×10^{12}	2.14	3.76	3.011

three samples [see Figs. 4(d)–4(f)], where data are presented $>3\,\mathrm{MW/cm^2}$ power density. In this context, the excitation carrier density has been estimated from the power density of the laser measured during the experiment. The laser spot is tightly focused on the sample surface to transfer maximum power to the system, and the excitation carrier density has been estimated using the equation [30]

$$n_0 = \frac{\text{power density} \times \tau o \times \left(\frac{I}{I_0}\right) \times A}{E}, \quad (2)$$

where τ_0 is the timescale beyond which the excitons are expected to achieve thermal equilibrium in ML TMD materials ($\sim$1 ps), A is the absorbance of suspended ML WS$_2$ at 2.33 eV (532 nm) excitation, which is $\sim$19% [11]. Furthermore, the interference from the substrate affecting the excitation intensity has been estimated using

$$\left(\frac{I}{I_0}\right) = \frac{4}{(1 + \text{r.i.})^2}, \quad (3)$$

where r.i. is the refractive index of the substrate material at 532 nm laser excitation. Accordingly, we have extracted the excitation carrier density from incident laser power density for all three substrates. Thereafter, the RBC of the excitonic peak position is noticed at an elevated $c_d \sim 3.267 \times 10^{12}\,\mathrm{cm^{-2}}$ ($2.267 \times 10^{12}\,\mathrm{cm^{-2}}$) for $P_d \sim 9.73\,\mathrm{MW/cm^2}$ (8.55 MW/cm^2) in the case of WS$_2$ on the SiO$_2$/Si (Al$_2$O$_3$) substrate. Here, Region I (green shaded region) is described as the lower carrier density regime, where excitons exhibit an insulating gas phase. On the contrary, excitons transform into the conducting EHP phase in Region II (yellow shaded region), which is denoted as the higher carrier density regime. The appearance of RBC and abrupt fall of I_{PL} reconfirm the absence of bound excitons and creation of separate charged quasiparticles beyond the Mott point in the case of ML WS$_2$ on Al$_2$O$_3$ and SiO$_2$ substrates. For a comparative discussion, we have also tabulated all the extracted parameters regarding the Mott transition in Table II. On the contrary, for the metallic Au substrate [see Fig. 4(f)], the excitonic peak gets only redshifted from the beginning with increasing P_d (or c_d), and RBC, as well as the Mott transition, is not observed even at a high P_d due to the direct charge transfer from ML WS$_2$ to the Au layer. For the metallic Au substrate, I_{PL} [see Fig. 4(c)] increases rapidly in the beginning and then starts to decrease linearly with increasing P_d due to lower density of exciton formation in WS$_2$.

The occurrence of RBC due to the formation of EHP beyond the Mott density can be analyzed with an analogy of attraction-repulsion crossover of exciton-exciton interactions in 2D systems [36] (detailed discussion in Appendix C). In our case, the energy is shifted due to excitonic interactions for the entire optical excitation range and can be modeled using two power laws, analogous with the Lennard-Jones potential between atoms, which can be written as

$$\Delta E = \varepsilon \left[\left(\frac{r_0}{r_s}\right)^{k1} - \left(\frac{r_0}{r_s}\right)^{k2} \right]. \quad (4)$$

Here, ε, r_0, $k1$, and $k2$ are the fitting parameters, where r_s is the average distance between excitons, r_0 is the distance where energy shift (ΔE) becomes zero, and ε represents the ΔE value at the Mott transition point where attraction repulsion crossover between excitons takes place. We have fitted our experimental data with Eq. (4) [see Figs. 5(a) and 5(b)] for the dielectric substrates (Al$_2$O$_3$ and SiO$_2$). The extracted parameters are $\varepsilon = 39.24\,\mathrm{meV}$, $r_0 = 3.011\,\mathrm{nm}$, $k1 = 8.25$, and $k2 = 1.52$, for Al$_2$O$_3$ and $\varepsilon = 54.25\,\mathrm{meV}$, $r_0 = 2.686\,\mathrm{nm}$, $k1 = 3.69$, and $k2 = 0.71$, for SiO$_2$, which are well in agreement with the previously reported results on chemical-vapor-deposition-grown ML WS$_2$ on a sapphire substrate [36].

The exciton Bohr radius (r_B) can be extracted from the interexcitonic distance around the Mott point, and usually, the interexcitonic distance inside atomically thin materials varies with the carrier density as $r_s = (1/\pi n)^{1/2}$ [30]. With increasing photoexcitation, the excessive population of carriers in a specific area reduces interexciton separation in the high-density regime. Essentially, at a carrier density of $3.267 \times 10^{12}\,\mathrm{cm^{-2}}$, the interexcitonic distances are reduced to $\sim$3.12 nm, which is around the exciton Bohr radius of WS$_2$. At this extremum, excitons lose their identity and fail to be distinguished as e-h pairs. Consequently, the whole exciton population starts to behave as free carriers, making the resultant EHP state by losing their binding energies to zero [36,55]. The obtained Bohr radius values from Lennard-Jones potential fittings reveal r_B of ML WS$_2$ as $r_B = 2.686\,\mathrm{nm}$ (3.011 nm) for the SiO$_2$ (Al$_2$O$_3$) substrate. In the case of the Au substrate, we are unable to calculate the Bohr radius of WS$_2$, as the Mott point is absent here. Now the variation of Mott points, as well as the Bohr radius of 2D ML WS$_2$, has a correlation with the substrate screening effect. The 2D dielectric constant (ε_q^{2d}), considering the surrounding medium, can be expressed as

$$\varepsilon_q^{2d} = \frac{k_a + k_b}{2} + qd\frac{k_{2D} - 1}{2}, \quad (5)$$

where k_a and k_b are the dielectric constant of upper and lower dielectric materials, and k_{2D} is the dielectric constant of ML WS$_2$ [56]. Using the 2D model, we can evaluate the screened dielectric constant, which is more for high-k dielectric substrates. This in turn lowers the binding energy of excitons (E_b^X) and increases the excitonic Bohr radius defined by $r_B = \varepsilon_q^{2d}\hbar^2/\mu e^2$, where $\mu = (m_e m_h/m_e + m_h)$ is the reduced effective mass of exciton. From the Lennard-Jones potential fit, we have extracted r_B for SiO$_2$ to be lower than
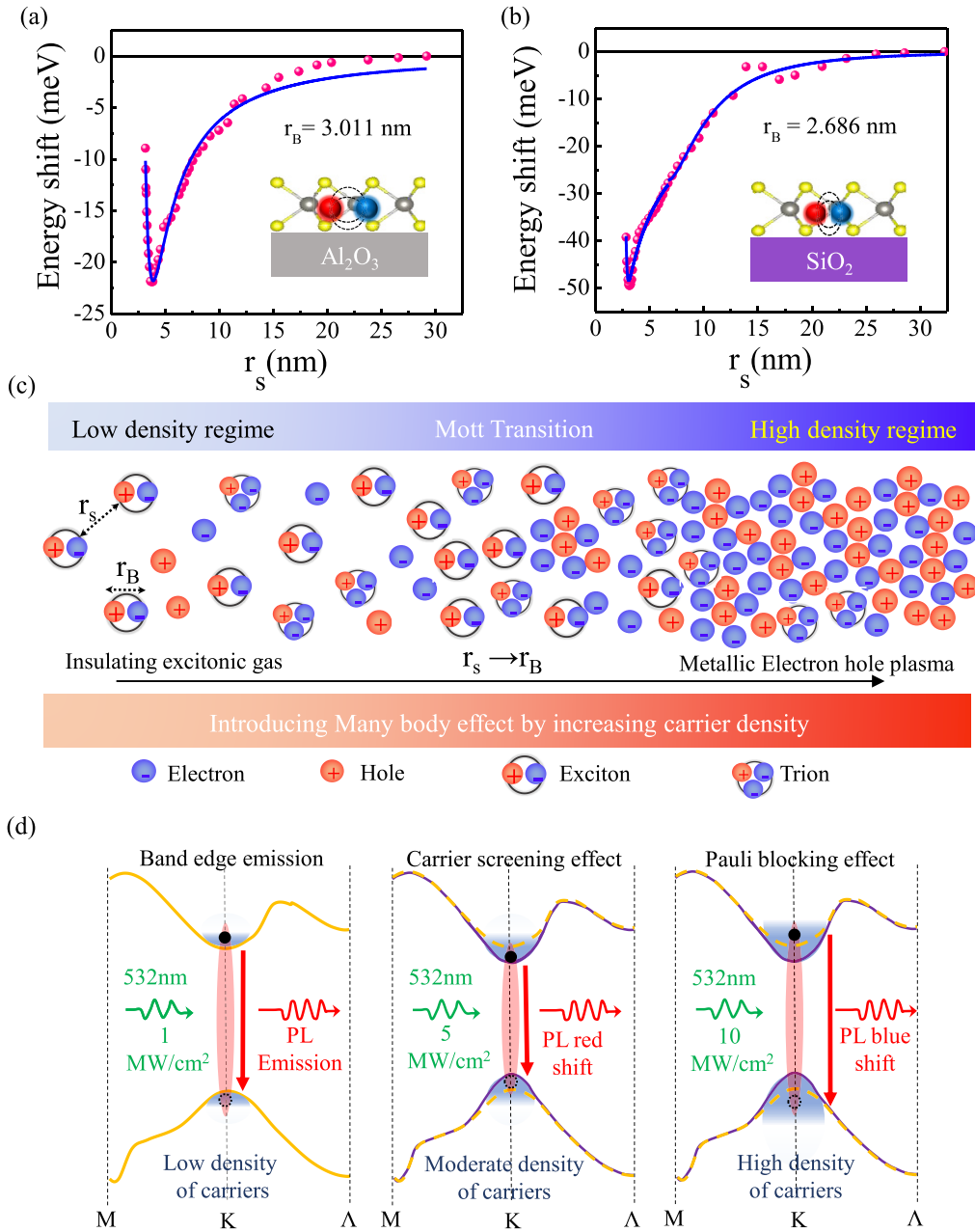
FIG. 5. Exciton energy shift (ΔE) variation with respect to average distance between excitons (r_s) for (a) Al_2O_3 and (b) SiO_2/Si substrates. The curves are fitted with the Lennard-Jones potential, and the excitonic Bohr radii are extracted for each substrate. In the inset of the two figures, the schematic representations of the exciton Bohr radius variation with dielectric environment alteration are illustrated. (c) Schematic of the increasing exciton density-induced many-body effect in transition metal dichalcogenide (TMD) materials leading to Mott transition in WS_2. (d) Schematic illustration of photoluminescence (PL) redshift-blueshift crossover due to interplay between band renormalization and the Pauli blocking effect of carriers.

that for Al_2O_3, contributing to the substrate screening effect, which has a great impact on deciding the Mott transition point with the variation of dielectric substrate. The dielectric screening-induced exciton Bohr radius distinction is illustrated schematically in the bottom right inset of Figs. 5(a) and 5(b).

In a nutshell, the RBC and Mott transition phenomena of excitonic resonance energy with increasing P_d (or c_d) are the result of different many-body effects acting synergistically on the excitonic quasiparticles in ML WS_2, as depicted schemat-

ically in Figs. 5(c) and 5(d). At a lower P_d, the screening of Coulomb repulsion among similar charges with increase in c_d leads to decrease in the electronic bandgap, which is generally referred to as bandgap renormalization (ΔE_g^{BGR}) [27–29]. On the contrary, photogenerated excess carriers can screen the Coulomb attraction between electrons and holes, promoting the reduction of exciton binding energy (ΔE_b^{CP}). Therefore, the position of excitonic transition with increasing carrier population is a consequence of the competitive behavior between the bandgap reduction (ΔE_g) causing a redshift

and the binding energy reduction (ΔE_b) causing a blueshift in PL resonance energy. It is important to note here that E_g decreases faster than E_b, so the excitonic peak undergoes a redshift initially with increasing laser power [28,57]. Further increment of laser power leads to the high carrier density regime, where the number of charge carriers increases to a higher value, and due to strong interaction between them, the Mott transition can occur at $n > 2 \times 10^{12}$ cm^{-2} [29]. In the Mott transition regime, another phenomenon comes into play, namely, Pauli blocking of carriers, which typically contributes to the blueshift of exciton resonance beyond the Mott point [52]. With further increase in P_d, the states near the CB edge start to fill up. This phase-space filling effect (or Moss-Brustein effect) [29] is governed by the Pauli exclusion principle due to the fermionic nature of electrons and holes, thus eventually pushing the free carriers to occupy higher energy states of the CB [58]. Consequently, an apparent bandgap increase phenomenon, also referred to as Pauli blocking effect (ΔE_g^{PB}) with reduced exciton oscillator strength, and corresponding decrement in exciton binding energy (ΔE_b^{PSF}) is observed. Therefore, the pivotal expressions for realizing the RBC point can be written as

$$\Delta E_g = \Delta E_g^{\text{BGR}} + \Delta E_g^{\text{PB}}, \qquad (6)$$

$$\Delta E_b = \Delta E_b^{\text{CP}} + \Delta E_b^{\text{PSF}}. \qquad (7)$$

As a result, the interplay among all these diverse many-body effects controls the optical transition rule in ML WS$_2$ with variable substrates, paving the way for added flexibility in designing optical devices for futuristic 2D-material-based photonic systems.

IV. SUMMARY AND CONCLUSIONS

In conclusion, a correlation between optical doping-induced charge screening and substrate-induced dielectric screening has been investigated in monolayer 2D WS$_2$ flakes, with the observed properties explained in the context of many-body phenomena that come into play at an elevated photoexcited carrier density ($\sim 10^{12}$ cm^{-2} and above). A comparative study of steady-state emission and Raman spectroscopy for dielectric and metallic substrates at a lower carrier density reveals substrate-induced unintentional doping and dielectric screening on ML WS$_2$, as corroborated with our DFT results. Moreover, with increasing carrier density, a clear redshift of excitonic resonance energy is observed for all three substrates, originating from carrier screening and long-range exciton-exciton attraction effects. However, in the case of dielectric substrates, around the Mott transition densities ($n_M \sim 3 \times 10^{12}$ cm^{-2}), a clear blueshift is noticed, giving rise to RBC phenomena. The observed RBC phenomena on dielectric substrates are attributed to the combinatorial effect of Pauli blocking and short-range exciton-exciton repulsion, which is, however, absent for the metallic Au substrate due to efficient charge transfer from WS$_2$. The observation could be explained by the Lennard-Jones potential model for two dielectric substrates (SiO$_2$ and Al$_2$O$_3$), which also provides an estimate of the exciton Bohr radii for ML WS$_2$. The reported in-depth introspections on the synergistic behavior of the PL

emission profile, RBC phenomena, and Mott transition points for a range of substrates are appealing in designing of numerous 2D TMD photonic devices operating at a wide excitation power regime (0.14–12 MW/cm^2).

APPENDIX A: THEORETICAL ANALYSIS

The influence of different substrates on the electronic properties of WS$_2$ has been analyzed after investigating its interfaces with three different substrates, viz., (1) Al$_2$O$_3$/WS$_2$, (2) SiO$_2$/WS$_2$, and (3) Au [111]/WS$_2$. The optical properties of WS$_2$ will be a closely related function of the interlayer coupling and therein generate mutual charge transfer within the constituent layers. The density functional investigations of these three WS$_2$ substrate interfaces were carried out by using the spin-polarized calculations with norm-conserving projector augmented wave pseudopotentials, as implemented in the Vienna *Ab initio* Simulation Package (VASP). The exchange-correlation interactions were treated with the generalized gradient approximation with Perdew-Burke-Ernzerhof functions after incorporating the SOC. Interfacial dipolar van der Waals corrections were included via a semiempirical dispersion potential to the DFT energy functional according to the Grimme DFT-D2 method [59]. The cutoff energy for the plane-wave expansion was set as 500 eV, and a Monkhorst-Pack grid of $5 \times 5 \times 3$ was used for the Brillouin zone sampling for all calculations. The ionic positions and the lattice parameters were optimized by using the conjugate gradient algorithm until the Hellmann-Feynman force on each ion was <0.01 eV.

To reinvestigate substrate-induced doping effects on ML WS$_2$, we calculated the electronic band structure of all samples using DFT. According to our calculations, the up (red)- and down (blue)-spin channel projections of W-5d and both spin channel projections of S-3p orbitals (green) are presented for WS$_2$ monolayer in Fig. 3(i). The bonding and antibonding manifolds are populated by S-3p_x- and 3p_y-hybridized W-5d_{xz}, 5d_{yz}, and 5d_{xy}, and S-3p_z-hybridized W-5d_{x-y}^2 and W-5d_{3z-1}^2 states, respectively. The layer projections of Al$_2$O$_3$ and WS$_2$ (defined as interface 1) are presented in Figs. 3(ii) and 3(iii), respectively, with the color codes as defined in the respective figures. The interface, having the lowest interfacial lattice mismatch, has the least doping and thereby succeeds in generating a layer decoupling of excitonic quasiparticles. Interface 2 (WS$_2$-SiO$_2$), exhibits an increase of the n-type doping in this system as compared with the earlier one. Figures 3(iv) and 3(v) represent the layer projections of the SiO$_2$ and WS$_2$ levels of interface 2, respectively. Whereas the valence levels are mostly populated by the O-2p and hybridized W-5d and S-3p states, the CB is contributed by the Si-3s and 3p states, indicating transfer of electrons from Si-3s and 3p

to WS$_2$ via O-2p levels. Interface 3 (WS$_2$-Au), on the other hand, represents the largest amount of charge-transfer from the Au[111] surface to the WS$_2$ layer, and as a result, the entire interface acquires a metallic nature. Figures 3(vi) and 3(vii) illustrate the layer projections of Au[111] and WS$_2$ layers, indicating highly delocalized Au-5d and 6s levels around E_F, transferring the charges to the S-3p levels of WS$_2$ and thereby leading to highly hybridized Au and S levels. On the other hand, the DOSs for these three interfaces are depicted in Fig. S7(a) of the Supplemental Material [40]. As will be evident from an overall comparison of these two figures, there are monotonic incremental shifts of the E_F for these three interfaces toward the CB of the combined system, indicating a gradual increase of the n-type doping from the interface system 1 to 3, as corroborated with our Raman results. This increase of the n-type doping can be attributed to the increase of mutual charge transfer (electron) from the substrate to the ML WS$_2$. The extents of doping are seen to have an explicit relationship with the mismatch of lattice parameters of the constituent layers. The extent of interlayer charge transfer and thereby induced explicit n-type doping are more evident from the Fig. S7(b) of the Supplemental Material [40], where the converged charge-density distributions are presented. Gradual increase of charge transfer manifesting larger interfacial overlap of charge spheres from interface 1 to 3 is obvious from Figs. S7(b)(i)–S7(b)(iii) of the Supplemental Material [40].

APPENDIX B: DIELECTRIC SCREENING-INDUCED BAND RENORMALIZATION

According to Fig. 2(b), a clear PL peak shift is noticed, which is direct evidence of dielectric screening-induced band renormalization. At a relatively low excitation power (neglecting Pauli blocking effect), the electronic bandgap can be written as

$$E_g^X = E_g^{SPX} + \frac{E_g^{BGRX0}}{(k_{eff})^\beta}, \tag{B1}$$

where E_g^{SPX} is the electronic bandgap from the single particle model, E_g^{BGRX0} is the bandgap renormalisation term in vacuum, β is another scaling factor, and X represents quasiparticles generated inside WS$_2$. Hence, for a higher-k dielectric (Al$_2$O$_3$), the effect of band renormalization and hence E_g^X will be lesser than SiO$_2$ with a lower dielectric permittivity. On the other hand, the binding energy (E_b) of an excitonic quasiparticle reflects the Coulomb potential between the charges, which is screened further by the environmental dielectric [30]. The variation of binding energy of quasiparti-

cles with effective dielectric constant (k_{eff}) of the environment can be described by

$$E_b^X = \frac{E_b^{X0}}{(k_{eff})^\alpha}, \tag{B2}$$

where E_b^{X0} is binding energy in vacuum (without substrate), $k_{eff} = (k_1 + k_2)/2$ is the effective dielectric constant. Here, k_1 and k_2 are the dielectric constants of the top and bottom dielectric layers of the WS$_2$ flake, and α is the scaling factor. Thus, the binding energy of quasiparticles (E_b^X) will reduce with increasing dielectric constant of the environment causing a blueshift of energy. The optical bandgap or quasiparticle resonance energy can be described as

$$PL_X = E_g^X - E_b^X, \tag{B3}$$

$$PL_X = E_g^{SPX} + \frac{E_g^{BGRX0}}{(k_{eff})^\beta} - \frac{E_b^{X0}}{(k_{eff})^\alpha}. \tag{B4}$$

As E_b^X is more strongly affected via dielectric screening than E_g^X, a blueshift of the PL peak is observed for higher-k dielectric Al$_2$O$_3$ than SiO$_2$.

APPENDIX C: MODELING OF RBC PHENOMENA

Exciton-exciton interactions are modulated by generating substantial carrier density inside ML WS$_2$, which initiates the transition from an insulating excitonic state to the metallic EHP state. Like the hydrogen atom, the attractive exciton-exciton interaction matches with the long-range Lennard-Jones interaction between atoms. Mutual attraction between any two excitons reduces the energy required to form an additional exciton by an amount of the negative interaction potential energy, which results in the redshift of the PL resonance peak. Using the same analogy, the origin of the excitonic blueshift can be interpreted for higher carrier densities at a higher laser power. A large fraction of charge carriers creates the high density of bound excitons via reducing the interexcitonic distances, leading to the stronger exciton-exciton repulsion due to overlapping electronic orbitals. This process leads to positive interexciton potential energy, which is the plausible reason behind the excitonic blueshift. Considering excitons as rigid bodies, the critical densities at which the excitons are closely packed can be determined as $n_e \pi r_s^2 \sim 1$, where n_e is the density of the excitons, and r_s is the average distance between excitons [30]. Around the Mott transition point, the exciton density becomes so high that the interexcitonic distance reduces to the excitonic Bohr radius (r_B) of the material.

[1] Z. Yu, Y. Pan, Y. Shen, Z. Wang, Z.-Y. Ong, T. Xu, R. Xin, L. Pan, B. Wang, L. Sun, J. Wang, G. Zhang, Y. W. Zhang, Y. Shi, and X. Wang, Towards intrinsic charge transport in monolayer molybdenum disulfide by defect and interface engineering, Nat. Commun. **5**, 5290 (2014).

[2] D. Ovchinnikov, A. Allain, Y. Huang, D. Dumcenco, and A. Kis, Electrical transport properties of single-layer WS$_2$, ACS Nano **8**, 8174 (2014).

[3] J. Sun, H. Hu, D. Pan, S. Zhang, and H. Xu, Selectively depopulating valley-polarized excitons in monolayer MoS$_2$ by local chirality in single plasmonic nanocavity, Nano Lett. **20**, 4953 (2020).

[4] W. Liu, B. Lee, C. H. Naylor, H.-S. Ee, J. Park, A. T. C. Johnson, and R. Agarwal, Strong exciton-plasmon coupling in MoS$_2$ coupled with plasmonic lattice, Nano Lett. **16**, 1262 (2016).

[5] F. Withers, O. Del Pozo-Zamudio, A. Mishchenko, A. P. Rooney, A. Gholinia, K. Watanabe, T. Taniguchi, S. J. Haigh, A. K. Geim, A. I. Tartakovskii, and K. S. Novoselov, Light-emitting diodes by band-structure engineering in van der Waals heterostructures, Nat. Mater. **14**, 301 (2015).

[6] B. W. H. Baugher, H. O. H. Churchill, Y. Yang, and P. Jarillo-Herrero, Optoelectronic devices based on electrically tunable *p-n* diodes in a monolayer dichalcogenide, Nat. Nanotechnol. **9**, 262 (2014).

[7] H.-Y. Lan, Y.-H. Hsieh, Z.-Y. Chiao, D. Jariwala, M.-H. Shih, T.-J. Yen, O. Hess, and Y.-J. Lu, Gate-tunable plasmon-enhanced photodetection in a monolayer MoS_2 phototransistor with ultrahigh photoresponsivity, Nano Lett. **21**, 3083 (2021).

[8] J. R. Schaibley, H. Yu, G. Clark, P. Rivera, J. S. Ross, K. L. Seyler, W. Yao, and X. Xu, Valleytronics in 2D materials, Nat. Rev. Mater. **1**, 16055 (2016).

[9] K. F. Mak, K. He, J. Shan, and T. F. Heinz, Control of valley polarization in monolayer MoS_2 by optical helicity, Nat. Nanotechnol. **7**, 494 (2012).

[10] Y. Li, J. Ludwig, T. Low, A. Chernikov, X. Cui, G. Arefe, Y. D. Kim, A. M. van der Zande, A. Rigosi, H. M. Hill, S. H. Kim, J. Hone, Z. Li, D. Smirnov, and T. F. Heinz, Valley Splitting and Polarization by the Zeeman Effect in Monolayer $MoSe_2$, Phys. Rev. Lett. **113**, 266804 (2014).

[11] Y. Li, A. Chernikov, X. Zhang, A. Rigosi, H. M. Hill, A. M. van der Zande, D. A. Chenet, E.-M. Shih, J. Hone, and T. F. Heinz, Measurement of the optical dielectric function of monolayer transition-metal dichalcogenides: MoS_2, $MoSe_2$, WS_2, and WSe_2, Phys. Rev. B **90**, 205422 (2014).

[12] L. Su, Y. Yu, L. Cao, and Y. Zhang, Effects of substrate type and material-substrate bonding on high-temperature behavior of monolayer WS_2, Nano Res. **8**, 2686 (2015).

[13] Z. He, X. Wang, W. Xu, Y. Zhou, Y. Sheng, Y. Rong, J. M. Smith, and J. H. Warner, Revealing defect-state photoluminescence in monolayer WS_2 by cryogenic laser processing, ACS Nano **10**, 5847 (2016).

[14] Y. Lin, X. Ling, L. Yu, S. Huang, A. L. Hsu, Y.-H. Lee, J. Kong, M. S. Dresselhaus, and T. Palacios, Dielectric screening of excitons and trions in single-layer MoS_2, Nano Lett. **14**, 5569 (2014).

[15] M. Buscema, G. A. Steele, H. S. J. van der Zant, and A. Castellanos-Gomez, The effect of the substrate on the Raman and photoluminescence emission of single-layer MoS_2, Nano Res. **7**, 561 (2014).

[16] B. Liu, W. Zhao, Z. Ding, I. Verzhbitskiy, L. Li, J. Lu, J. Chen, G. Eda, and K. P. Loh, Engineering bandgaps of monolayer MoS_2 and WS_2 on fluoropolymer substrates by electrostatically tuned many-body effects, Adv. Mater. **28**, 6457 (2016).

[17] Y. Yu, Y. Yu, C. Xu, Y. Q. Cai, L. Su, Y. Zhang, Y. W. Zhang, K. Gundogdu, and L. Cao, Engineering substrate interactions for high luminescence efficiency of transition-metal dichalcogenide monolayers, Adv. Funct. Mater. **26**, 4733 (2016).

[18] Q. Zhang, Z. Chang, G. Xu, Z. Wang, Y. Zhang, Z. Q. Xu, S. Chen, Q. Bao, J. Z. Liu, Y. W. Mai, W. Duan, M. S. Fuhrer, and C. Zheng, Strain relaxation of monolayer WS_2 on plastic substrate, Adv. Funct. Mater. **26**, 8707 (2016).

[19] S. Lippert, L. M. Schneider, D. Renaud, K. N. Kang, O. Ajayi, J. Kuhnert, M.-U. Halbich, O. M. Abdulmunem, X. Lin, K. Hassoon, S. Edalati-Boostan, Y. D. Kim, W. Heimbrodt,

E.-H. Yang, J. C. Hone, and A. Rahimi-Iman, Influence of the substrate material on the optical properties of tungsten diselenide monolayers, 2D Mater. **4**, 025045 (2017).

[20] Y. Kajino, K. Oto, and Y. Yamada, Modification of optical properties in monolayer WS_2 on dielectric substrates by Coulomb engineering, J. Phys. Chem. C **123**, 14097 (2019).

[21] S. Mouri, Y. Miyauchi, and K. Matsuda, Tunable photoluminescence of monolayer MoS_2 via chemical doping, Nano Lett. **13**, 5944 (2013).

[22] X. Gan, Y. Gao, K. Fai Mak, X. Yao, R.-J. Shiue, A. van der Zande, M. E. Trusheim, F. Hatami, T. F. Heinz, J. Hone, and D. Englund, Controlling the spontaneous emission rate of monolayer MoS_2 in a photonic crystal nanocavity, Appl. Phys. Lett. **103**, 181119 (2013).

[23] D. Jena and A. Konar, Enhancement of Carrier Mobility in Semiconductor Nanostructures by Dielectric Engineering, Phys. Rev. Lett. **98**, 136805 (2007).

[24] H.-P. Komsa and A. V. Krasheninnikov, Effects of confinement and environment on the electronic structure and exciton binding energy of MoS_2 from first principles, Phys. Rev. B **86**, 241201(R) (2012).

[25] Y. Chen, W. Wen, Y. Zhu, N. Mao, Q. Feng, M. Zhang, H. P. Hsu, J. Zhang, Y. S. Huang, and L. Xie, Temperature-dependent photoluminescence emission and Raman scattering from $Mo_{1−x}W_xS_2$ monolayers, Nanotechnology **27**, 445705 (2016).

[26] Z. Ye, T. Cao, K. O'Brien, H. Zhu, X. Yin, Y. Wang, S. G. Louie, and X. Zhang, Probing excitonic dark states in single-layer tungsten disulphide, Nature (London) **513**, 214 (2014).

[27] M. M. Ugeda, A. J. Bradley, S.-F. Shi, F. H. da Jornada, Y. Zhang, D. Y. Qiu, W. Ruan, S.-K. Mo, Z. Hussain, Z.-X. Shen, F. Wang, S. G. Louie, and M. F. Crommie, Giant bandgap renormalization and excitonic effects in a monolayer transition metal dichalcogenide semiconductor, Nat. Mater. **13**, 1091 (2014).

[28] A. Chernikov, C. Ruppert, H. M. Hill, A. F. Rigosi, and T. F. Heinz, Population inversion and giant bandgap renormalization in atomically thin WS_2 layers, Nat. Photonics **9**, 466 (2015).

[29] P. D. Cunningham, A. T. Hanbicki, K. M. McCreary, and B. T. Jonker, Photoinduced bandgap renormalization and exciton binding energy reduction in WS_2, ACS Nano **11**, 12601 (2017).

[30] E. J. Sie, A. J. Frenzel, Y.-H. Lee, J. Kong, and N. Gedik, Intervalley biexcitons and many-body effects in monolayer MoS_2, Phys. Rev. B **92**, 125417 (2015).

[31] K. Seeger, *Semiconductor Physics* (Springer, Berlin, Heidelberg, 2004).

[32] B. H. Moon, J. J. Bae, G. H. Han, H. Kim, H. Choi, and Y. H. Lee, Anomalous conductance near percolative metal-insulator transition in monolayer MoS_2 at low voltage regime, ACS Nano **13**, 6631 (2019).

[33] P. D. Patil, S. Ghosh, M. Wasala, S. Lei, R. Vajtai, P. M. Ajayan, A. Ghosh, and S. Talapatra, Gate-induced metal-insulator transition in 2D van der Waals layers of copper indium selenide based field-effect transistors, ACS Nano **13**, 13413 (2019).

[34] B. H. Moon, J. J. Bae, M.-K. Joo, H. Choi, G. H. Han, H. Lim, and Y. H. Lee, Soft Coulomb gap and asymmetric scaling towards metal-insulator quantum criticality in multilayer MoS_2, Nat. Commun. **9**, 2052 (2018).

[35] M. Karmakar, S. Mukherjee, S. K. Ray, and P. K. Datta, Electron-hole plasma formation dynamics observed through

exciton-plasma interactions in transition metal dichalcogenides, Phys. Rev. B **104**, 075446 (2021).

[36] E. J. Sie, A. Steinhoff, C. Gies, C. H. Lui, Q. Ma, M. Rösner, G. Schönhoff, F. Jahnke, T. O. Wehling, Y.-H. Lee, J. Kong, P. Jarillo-Herrero, and N. Gedik, Observation of exciton redshift-blueshift crossover in monolayer WS₂, Nano Lett. **17**, 4210 (2017).

[37] W. Langbein, S. Hallstein, H. Kalt, R. Nötzel, and K. Ploog, Negative-differential band-gap renormalization in type-II GaAs/AlAs superlattices, Phys. Rev. B **51**, 1946 (1995).

[38] G. R. Olbright, W. S. Fu, J. F. Klem, H. M. Gibbs, G. Khitrova, R. Pon, B. Fluegel, K. Meissner, N. Peyghambarian, R. Binder, I. Galbraith, and S. W. Koch, Nonlinear optical properties of type-II quantum wells, Phys. Rev. B **44**, 3043 (1991).

[39] A. Chernikov, T. C. Berkelbach, H. M. Hill, A. Rigosi, Y. Li, O. B. Aslan, D. R. Reichman, M. S. Hybertsen, and T. F. Heinz, Exciton Binding Energy and Nonhydrogenic Rydberg Series in Monolayer WS₂, Phys. Rev. Lett. **113**, 076802 (2014).

[40] See Supplemental Material at http://link.aps.org/supplemental/10.1103/PhysRevMaterials.5.124001 for detailed optical analysis for power-dependent PL and dielectric screening effect inside WS2, including Figs. S1−S7.

[41] H. Li, J. Wu, X. Huang, G. Lu, J. Yang, X. Lu, Q. Xiong, and H. Zhang, Rapid and reliable thickness identification of two-dimensional nanosheets using optical microscopy, ACS Nano **7**, 10344 (2013).

[42] H. Li, G. Lu, Z. Yin, Q. He, H. Li, Q. Zhang, and H. Zhang, Optical identification of single- and few-layer MoS₂ sheets, Small **8**, 682 (2012).

[43] N. Peimyoo, W. Yang, J. Shang, X. Shen, Y. Wang, and T. Yu, Chemically driven tunable light emission of charged and neutral excitons in monolayer WS₂, ACS Nano **8**, 11320 (2014).

[44] S. Li, H. Miyazaki, H. Song, H. Kuramochi, S. Nakaharai, and K. Tsukagoshi, Quantitative Raman spectrum and reliable thickness identification for atomic layers on insulating substrates, ACS Nano **6**, 7381 (2012).

[45] A. Berkdemir, H. R. Gutiérrez, A. R. Botello-Méndez, N. Perea-López, A. L. Elías, C.-I. Chia, B. Wang, V. H. Crespi, F. López-Urías, J. Charlier, H. Terrones, and M. Terrones, Identification of individual and few layers of WS₂ using Raman spectroscopy, Sci. Rep. **3**, 1755 (2013).

[46] B. Chakraborty, A. Bera, D. V. S. Muthu, S. Bhowmick, U. V. Waghmare, and A. K. Sood, Symmetry-dependent phonon renormalization in monolayer MoS₂ transistor, Phys. Rev. B **85**, 161403(R) (2012).

[47] J. Robertson, High dielectric constant oxides, Eur. Phys. J. Appl. Phys. **28**, 265 (2004).

[48] M. S. Kim, S. J. Yun, Y. Lee, C. Seo, H. Han, K. K. Kim, Y. H. Lee, and J. Kim, Biexciton emission from edges and grain boundaries of triangular WS₂ monolayers, ACS Nano **10**, 2399 (2016).

[49] A. Steinhoff, J.-H. Kim, F. Jahnke, M. Rösner, D.-S. Kim, C. Lee, G. H. Han, M. S. Jeong, T. O. Wehling, and C. Gies, Efficient excitonic photoluminescence in direct and indirect band gap monolayer MoS₂, Nano Lett. **15**, 6841 (2015).

[50] G. Plechinger, P. Nagler, J. Kraus, N. Paradiso, C. Strunk, C. Schüller, and T. Korn, Identification of excitons, trions and biexcitons in single-layer WS₂, Phys. Status Solidi RRL, **9**, 457 (2015).

[51] X. Xu, L. Li, M. Yang, Q. Guo, Y. Wang, X. Li, X. Zhuang, and B. Liang, Localized state effect and exciton dynamics for monolayer WS₂, Opt. Express **29**, 5856 (2021).

[52] D. Huang, J. I. Chyi, and H. Morkoç, Carrier effects on the excitonic absorption in GaAs quantum-well structures: Phase-space filling, Phys. Rev. B **42**, 5147 (1990).

[53] T. Zhang and J. Wang, Defect-enhanced exciton-exciton annihilation in monolayer transition metal dichalcogenides at high exciton densities, ACS Photonics **8**, 2770 (2021).

[54] Y. Yu, Y. Yu, C. Xu, A. Barrette, K. Gundogdu, and L. Cao, Fundamental limits of exciton-exciton annihilation for light emission in transition metal dichalcogenide monolayers, Phys. Rev. B **93**, 201111 (2016).

[55] R. Zimmermann, Nonlinear optics and the Mott transition in semiconductors, Phys. Status Solidi **146**, 371 (1988).

[56] M. L. Trolle, T. G. Pedersen, and V. Véniard, Model dielectric function for 2D semiconductors including substrate screening, Sci Rep. **7**, 39844 (2017).

[57] X. Fan, W. Zheng, H. Liu, X. Zhuang, P. Fan, Y. Gong, H. Li, X. Wu, Y. Jiang, X. Zhu, Q. Zhang, H. Zhou, W. Hu, X. Wang, X. Duan, and A. Pan, Nonlinear photoluminescence in monolayer WS₂: parabolic emission and excitation fluence-dependent recombination dynamics, Nanoscale **9**, 7235 (2017).

[58] A. Amo, M. D. Martín, L. Via, A. I. Toropov, and K. S. Zhuravlev, Photoluminescence dynamics in GaAs along an optically induced Mott transition, J. Appl. Phys. **101**, 081717 (2007).

[59] S. Grimme, J. Antony, S. Ehrlich, and H. Krieg, A consistent and accurate *ab initio* parametrization of density functional dispersion correction (DFT-D) for the 94 elements H-Pu, J. Chem. Phys. **132**, 154104 (2010).